JGR Solid Earth

Key Points:
- We deployed a linear dense array of 8 km in length across the Chenghai fault that is critical to constrain the fault zone depth
- Based on teleseismic travel times and ambient noise tomography, we found a low-velocity zone of 3.4 km in width associated with the fault
- Ambient noise tomography showed that the low-velocity zone extends to 1.5 km in depth, consistent with teleseismic travel times

Fine Structure of the Chenghai Fault Zone, Yunnan, China, Constrained From Teleseismic Travel Time and Ambient Noise Tomography

Hongfeng Yang[1] , Yaohui Duan[1], Junhao Song[1] , Xiaohuan Jiang[2], Xiaofeng Tian[3] , Wei Yang[4], Weitao Wang[4], and Jun Yang[5]

[1]Earth System Science Programme, Faculty of Science, The Chinese University of Hong Kong, Shatin, Hong Kong, [2]Shenzhen Research Institute, The Chinese University of Hong Kong, Shenzhen, China, [3]Center of Geophysical Exploration, China Earthquake Administration, Zhengzhou, China, [4]Key Laboratory of Seismic Observation and Geophysical Imaging, Institute of Geophysics, China Earthquake Administration, Beijing, China, [5]West Yunnan Earthquake Forecasting Experiment Site, China Earthquake Administration, Dali, China

Abstract To derive high-resolution fault zone (FZ) structure of the Chenghai fault in Yunnan, southwestern China, we deployed a linear dense array crossing the fault from January to February 2018. The array consisted of 158 short-period (5 s) three-component instruments and spanned an aperture of ~8 km with average station spacing of 40–50 m. During the 1-month deployment, 20 teleseismic earthquakes with moment magnitudes larger than 5.5 and 41 local earthquakes were recorded. We first analyzed the travel times of P and S waves from teleseismic earthquakes to determine the boundaries of the FZ. After correcting the station-event geometry effects, teleseismic travel time differences between the reference station, and all other stations clearly marked a zone of 3.4 km in width with distinct travel time anomaly, suggesting a low-velocity zone (LVZ) surrounding the Chenghai fault. We then conducted ambient noise tomography and found that the S wave velocity of the LVZ was reduced by 60% and 40% compared to the northwest and southeast of the LVZ, respectively. Our ambient noise results suggested the LVZ extending to ~1.5 km in depth, consistent with the travel time anomalies of teleseismic earthquakes. Integrating ambient noise tomography with teleseismic travel times in a dense array with such an aperture is an effective approach for resolving FZ structure and depth extent.

Plain Language Summary High-resolution fault zone (FZ) structure and evolution are critical to understand earthquake physics. As the FZ width is usually on the order of 100 to 1,000 m, resolving the structure requires dense seismic arrays with small interstation spacing. One of the difficulties is to robustly constrain the depth extent by small-aperture arrays. Here we demonstrate that deployment of a large-aperture (8 km) array across a fault can robustly resolve the FZ structure and depth extent. Using the data acquired from a linear dense array crossing the Chenghai Fault in northwest Yunnan, China, we show that the low-velocity zone of the fault extends to 1.5 km from the results of ambient noise tomography, which are consistent with observations of travel times of body waves from teleseismic earthquakes. Such large-aperture array is an effective tool that enables integration of a variety of methods to robustly constrain high-resolution FZ structure.

1. Introduction

Crustal fault zones (FZ) host earthquakes, which may produce permanent damage and generate a low-velocity zone (LVZ). The LVZ properties have profound impacts on earthquake nucleation and rupture propagation (e.g., Ampuero et al., 2002; Ben-Zion & Sammis, 2003; Harris & Day, 1997; Weng et al., 2016). For instance, cracks and fluids in the damage zone may decrease the strength of faults (Caine et al., 1996; Eberhart-Phillips et al., 1995; Faulkner et al., 2010). If the fault is in the vicinity of industrial fluid injection, hydraulic properties of the damage FZ are critical on the occurrence of induced earthquakes (Yehya et al., 2018). Furthermore, it has been shown that the damage zone may lead to change of rupture mode and transition of rupture speed into supershear (Huang & Ampuero, 2011; Huang et al., 2014; Pelties et al., 2015). Moreover, dynamic rupture simulations suggest that the width and depth extent of the LVZ play critical roles in final rupture extents and thus the earthquake size (Weng et al., 2016), as well as in estimating

coseismic frictional properties from near fault ground deformation (Chen & Yang, 2020; Weng & Yang, 2018; Yao & Yang, 2020). In addition, temporal changes of velocities in the damaged FZ have been used as proxy of fault healing, which is significant to understand earthquake cycle and evolution of fault systems (Li et al., 1998; Vidale & Li, 2003). Therefore, high-resolution imaging of FZ structure will shed light on our understanding of earthquake physics (e.g., Yang, 2015).

Numerous efforts had been conducted to image FZs (Yang, 2015). For crustal faults, the most efficient methods were seismological investigations of data recorded on dense across-fault arrays. Travel times of body waves from local and teleseismic earthquakes had been proven efficient to determine the FZ boundaries (Li et al., 2007; Share et al., 2017; Yang et al., 2011; Yang et al., 2014). Waveform modeling of FZ trapped waves and FZ-reflected body waves had also been widely used to derive FZ structure (Cochran et al., 2009; Li et al., 1990; Peng et al., 2003; Yang & Zhu, 2010). As dense arrays have rapidly grown, travel time tomography and ambient noise tomography were also applied in imaging the FZs (Allam et al., 2014; Hillers et al., 2014; Lin et al., 2013; Zigone et al., 2014, 2019). Despite the recent progress in deriving FZ width and velocity contrast to the host rock, it was still challenging to robustly constrain the depth extent of the LVZ (Yang, 2015), as shown in previous investigations based on FZ trapped waves (Fohrmann et al., 2004; Lewis et al., 2005; Li & Vernon, 2001). By modeling the diffracted S waves around the edges of LVZ, Yang and Zhu (2010) were able to constrain the LVZ depth of the San Jacinto Fault. However, such approach highly depended on data quality, that is, available diffracted phases recorded by the small-aperture across-fault arrays.

In the early days, most across-fault arrays were deployed in a relatively small aperture, for example, a few hundreds of meters (Ben-Zion & Sammis, 2003; Li et al., 1990, 1994, 2004; Li & Vernon, 2001). The small aperture may lead to ambiguities in determining the LVZ width and depth based on travel times (Li et al., 2007; Yang et al., 2014). In 2004, a 4.5-km-long array was deployed across the Calico fault, enabling better constraints on the LVZ depth extent using travel times and waveforms (Cochran et al., 2009; Yang et al., 2011). It also allowed determination of a 1.3–1.5-km-wide LVZ, which exceeded the apertures of most other arrays. The results partly inspired deployment of dense across-fault arrays with larger aperture, for example, a 2-km-long profile across the northwest portion of the San Jacinto Fault (Share et al., 2019). Furthermore, FZ arrays were usually composed of high-frequency (4.5 Hz) geophones or short-period (2 Hz) instruments. Despite that long-period surface waves of large earthquakes were quite clear on these instruments (e.g., Wang et al., 2019), the frequency range of data to image the FZ was limited. Although a shallow structure of a few hundreds of meters in depth can be derived by high-frequency ambient noise tomography (Zigone et al., 2019), FZ structure at greater depth demanded longer-aperture arrays and lower-frequency waveforms.

In January 2018, we deployed a dense array crossing the Chenghai Fault in Yunnan, southwest China (Figure 1). The array consisted of 158 short-period (5 s) three-component instruments and spanned an aperture of ~8 km with average station spacing of 40–50 m. The instruments operated in the field for 1 month, from January to February 2018. To our best knowledge, this was the longest across-fault array with such frequency range, allowing us to derive high-resolution images of the FZ structure and its depth extent. In this study, we conducted ambient noise tomography to image the LVZ structure, with depth resolved down to ~2 km. The ambient noise tomographic images corroborated the results of teleseismic travel times and waveforms, indicating a 3.4 km LVZ associated with the Chenghai fault extending to a depth of 1.5 km.

## 2. Tectonic Setting and Dense Array Data

Due to the collision between the India and Eurasia plates, numerous faults were formed in the southeastern margin of the Tibetan Plateau, producing damaging earthquakes throughout Yunnan province. The Chenghai Fault (CHF) located in western Yunnan, oriented nearly N-S, extended ~200 km from Yongsheng in the north and intersected with the NW-SE trending Red River Fault (RRF) in the south (Figure 1). According to measurements of across-fault leveling and baseline, recent slip rates of the CHF were estimated to be ~4–10 mm/yr (Zhang & Liu, 2016). The largest earthquake that occurred on the CHF was the 1,515 $M7^3/_4$ Yongsheng earthquake (Wang et al., 2015; Zhou et al., 2004). Paleo-seismological records suggested more than 1,500 years of recurrence interval of $M7$ earthquakes on the CHF (Yu et al., 2005). In 2001, an $M6$ earthquake occurred in the north portion of the CHF. The
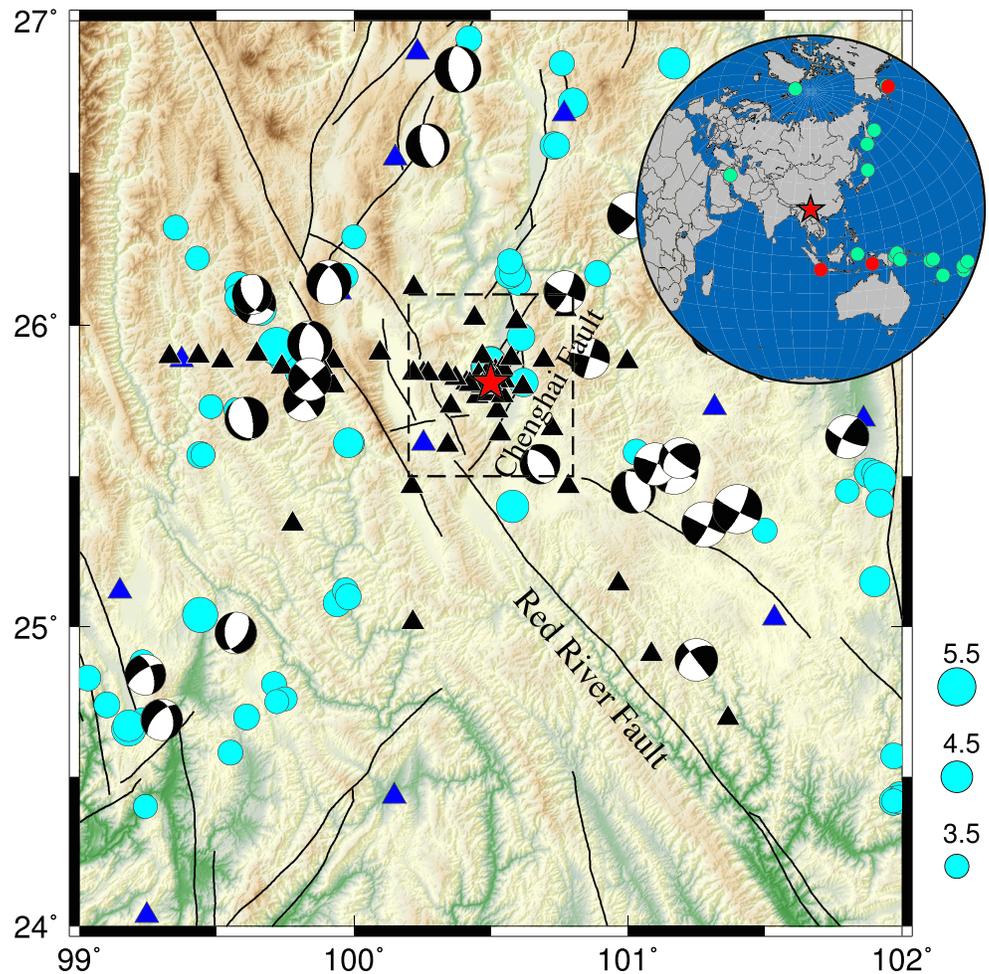
Figure 1. Location and faults (black lines) in the study region. Cyan dots represent earthquakes with magnitudes larger than 3.5 since 1970. Beach balls show moment tensor solutions from the GCMT database. Triangles show temporary (black) and permanent (blue) seismic stations. Red star denotes the location of the Binchuan airgun source. Dashed black box bounds the region that is shown in Figure 2. Locations of teleseismic earthquakes with magnitudes larger than 5.5 are shown in the inset map. Waveforms of three earthquakes (red) are shown in Figure 3. Fault location is from the database of active faults in China (Deng, 2004).

southern portion of the CHF had been suggested to be a seismic gap, capable of hosting earthquakes with magnitudes around 7 (e.g., Huang et al., 2018).

Besides the CHF, lots of other faults in the region were very active. There were at least four earthquakes with magnitudes greater than 7 in the past 500 years, with the most recent one being the 1996 Lijiang *M*7 earthquake (Zhou et al., 2004). The northern portion of the RRF and neighboring faults accommodated regional E-W crustal extension and N-S shortening due to the India-Eurasia collision (Allen et al., 1984) and had experienced strong earthquakes including the 1925 Dali *M*7 earthquake (Zhou et al., 2004). Because of frequent intermediate and large earthquakes in the region, seismic network had been rapidly growing in the past decade. Permanent stations were in the region with average spacing of ~60 km (blue triangles in Figure 1). To investigate temporal variations of crustal structure, an air gun source that can suddenly release large-volume compressed air and repeat in a short time was constructed in the Binchuan basin since April 2011 (red star in Figure 1). During 2013, thousands of air gun shots were conducted in Binchuan, Yunnan, with an average number of 30 per day. Signals of the air gun shots were nearly identical with cross-correlation coefficients larger than 0.99 (Chen et al., 2017), providing an unprecedented opportunity to continuously monitor the temporal variation of subsurface structure. For instance, clear diurnal and
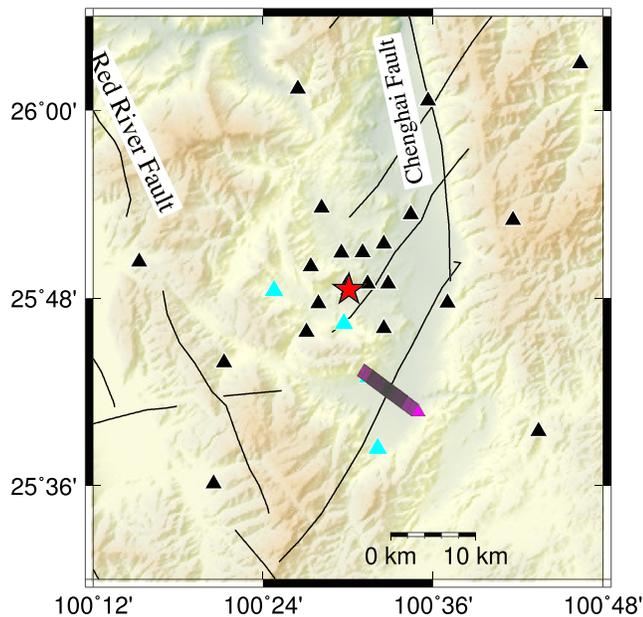
Figure 2. A map showing the location of local seismic stations (black triangles) and the airgun (star). Purple triangles show our dense array stations with average spacing of 40–50 m. Cyan colored triangles denote stations that show temporal variation in subsurface structure (Luan et al., 2016).

semidiurnal P and S wave velocity changes with amplitudes of 10^{-4} to 10^{-3} were derived from a 1-week data set of the air gun source in Binchuan (Wang et al., 2020).

After the air gun source was constructed in Binchuan, 40 intermediate-period seismic stations (Guralp CMG-40 T) had been deployed to complement the present Yunnan permanent seismic network (Figure 1). These stations had a sample rate of 100 points per second. We performed a systematic analysis of the waveform data recorded in 2013 to investigate the subsurface changes along the paths from the Binchuan air gun source to seismic stations (Luan et al., 2016). The results showed that four stations near the southern portion of the CHF had shown signatures of structural variation (Figure 2). We then selected this portion of the CHF and deployed a dense across fault array. The array was perpendicular to the fault orientation, crossed the geologically inferred fault trace, and spanned an aperture of ~8 km with average station spacing of 40–50 m. The array consisted of 158 EPS instruments, which had a corner frequency of 5 s for all three components. The instrument had a built-in battery and data logger and thus was very convenient to deploy in a large number. Sampling rates were set as 200 sample/s for all stations. During the 1-month deployment, 20 teleseismic earthquakes with magnitudes larger than 5.5, as well as 41 local earthquakes were recorded.

3. Data Analysis

3.1. Teleseismic Travel Times

Teleseismic waves sampled the structure beneath the array with a nearly vertical incident angle and thus the travel times of P and S waves were effective to reveal heterogeneous local structure (e.g., Cochran et al., 2009; Qiu et al., 2017; Share et al., 2019). We first manually picked all P wave arrivals for 14 teleseismic earthquakes with good signal-to-noise ratio (SNR) after filtering the waveform from 0.05 to 1.5 Hz. To remove the effects of station geometry, we calculated theoretical travel times using the 1-D IASP91 model (Kennett & Engdahl, 1991). Compared with the epicentral distances, our array aperture was very small so the theoretical travel times only slightly changed across the array (blue lines in Figure 3), depending on their back azimuths. Due to the imperfect 1-D velocity model, they were either advanced or delayed compared with our observations. Although the altitude changes across our array were minor (less than 150 m), our stations were located on elevations of ~1.5 km. We then corrected the topographic effects on the P wave theoretical travel times using $\frac{h_j}{v_{ref}}$, where h_j were elevations of individual stations, and $v_{ref} = 2$ km/s is the average P wave velocity of the shallow layer according to the tomography results using a few explosion sources in the region (Chen et al., 2016). After correction, the theoretical travel times were delayed a bit from the predictions by IASP91 (green lines in Figure 3), but were still different than our observations, reflecting heterogeneous local structure beneath the array. For instance, travel times of the direct P waves from an M_w7.9 Alaska earthquake showed clear variation across the array, with an obvious delay in observations at stations from −1 to 2.4 km in the profile (Figure 3a).

To focus on the local velocity structure, we derived the relative differential times across the array by the following two steps. We first subtracted the theoretical travel times from the observations on each station. Then we selected one reference station and further deducted the travel times between theoretical travel times and observations. As such, we can group all teleseismic earthquakes together (Figure 4a). Because we derived their relative delay times comparing with the reference station, the choice of reference stations did not change the results (Figure 4a). For instance, we had used three different reference stations, one in the northwest end, one in the center, and one in the southeast end of the array. The across-array delay patterns were identical, with only difference in values that were determined by the choice of the reference station.
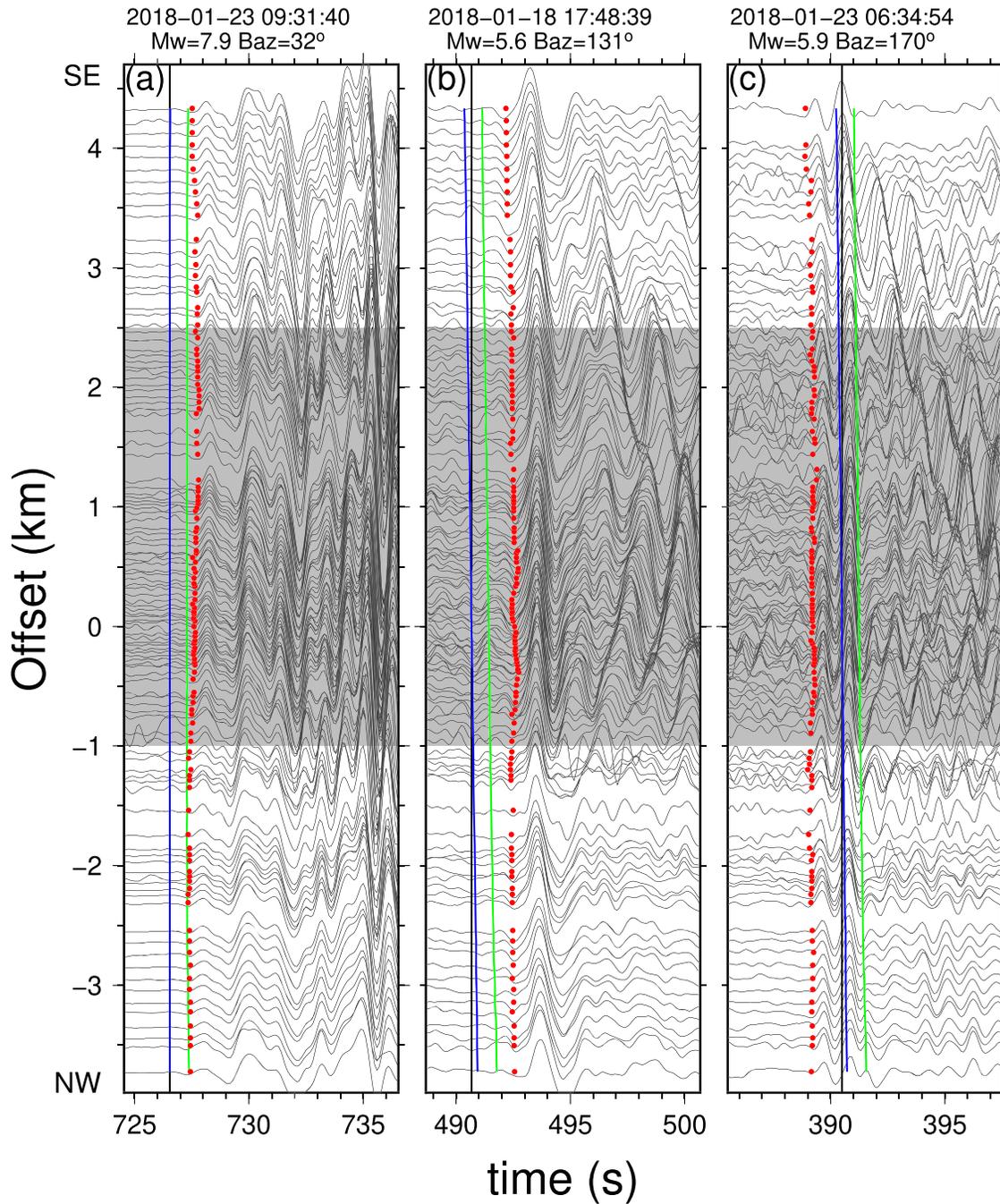
Figure 3. Waveforms of (a–c) three teleseismic earthquakes (locations shown in Figure 1) with theoretical (blue) and topography-corrected (green) travel times of *P* waves using the IASP91 model. Red dots represent our manually picked travel times. The waveforms are uniformly normalized across the array. *Y* axis shows the length of the array profile from northwest (NW) to southeast (SE), with 0 corresponding to inferred fault trace on surface (Deng, 2004). Gray area indicates the interpreted low-velocity zone according to travel time delays and waveform changes.

Similar to what were reported for local earthquakes (Li et al., 2007; Yang et al., 2011, 2014), the across-array travel time differences qualitatively marked a distinct LVZ beneath the array, starting from ~1 km in the northwest and having a width of ~3.4 km (Figure 4a). The arrivals systematically advanced from northwest to southeast across the profile. However, such advancing trend was interrupted near the station at ~1 km northwest to the geologically inferred fault trace (zero line for offset), and a reverse trend lasted until the
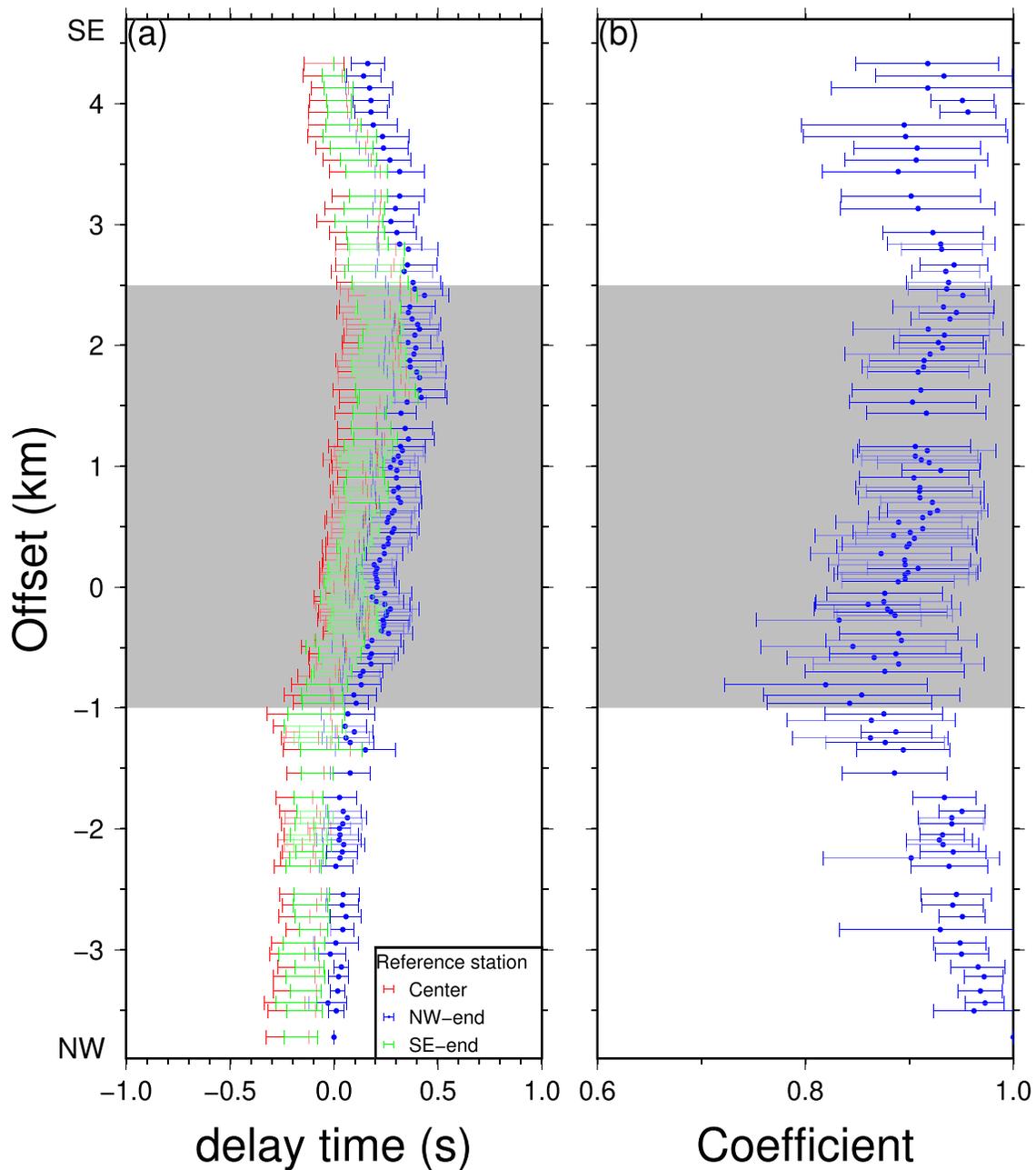
Figure 4. (a) Across-array delay times of P waves for all $M_w > 5.5$ teleseismic earthquakes after correcting event-station geometry and station elevations. Colors correspond to three different reference stations, one in the center and others in the two ends of the array. Error bars represent 1 standard deviation. (b) Cross-correlation coefficients of waveforms in a 4-s window using the reference station in the southwest end of the array.

station at ~2.4 km in the southeast (Figure 4a). In the southeast stations, the differential times become advanced again.

In addition to travel times, amplitudes of the direct P waves systematically changed across the array (Figure 3). Within the LVZ, the P wave amplitudes slightly increased compared with those at stations outside. As the direct teleseismic P waves are very clear and similar at each station, we cross correlated the waveforms in a 4-s time window (0.5 s before and 3.5 s after manually picked arrivals) around the P waves between each station and the reference station in the northwest end of the array. Cross-correlation coefficients (CC) were ~0.95 for stations in the northwestern side of the LVZ, reduced to 0.9 for stations inside
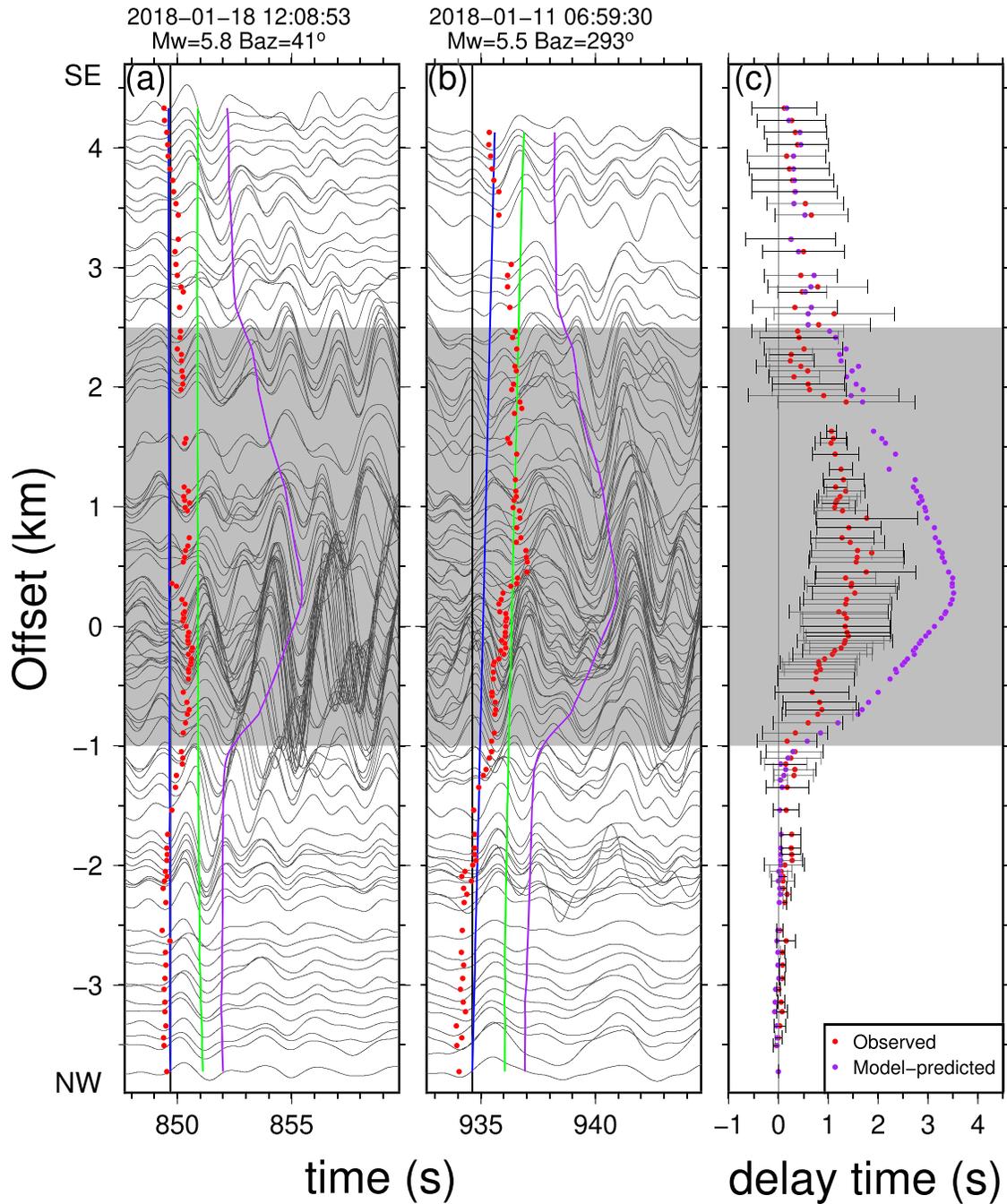
Figure 5. (a) and (b) Similar to Figure 3, except for *S* wave delay time analysis for two teleseismic events. (a) Red dots show the manually picked *S* wave arrivals. Theoretical arrivals before (blue) and after (green) correcting topography effects. Purple lines denote travel time predictions from the shear wave model obtained from ambient noise tomography. Gray shadows indicate the location of the low-velocity zone. (c) Observed (red) relative delay time of *S* arrivals after correcting station-event geometry and station elevation. Purple dots denote predicted *S* arrivals from the noise tomography model.

the LVZ, and slightly increased again for stations in the southeastern side of the LVZ (Figure 4b). The variation in the CC also marked the boundaries of the LVZ, consistent with travel time delays (Figure 4a).

Similar to the *P* waves, travel times of *S* waves exhibited the same delay pattern (Figure 5a), although *S* waves are less clear than *P* waves. We manually picked the *S* arrivals for six events with good SNR and performed the same station geometry and elevation correction (assuming $Vs = 1.2$ km/s) of travel times. The corrected travel times of *S* waves also showed large delays in stations inside the LVZ, with the same width
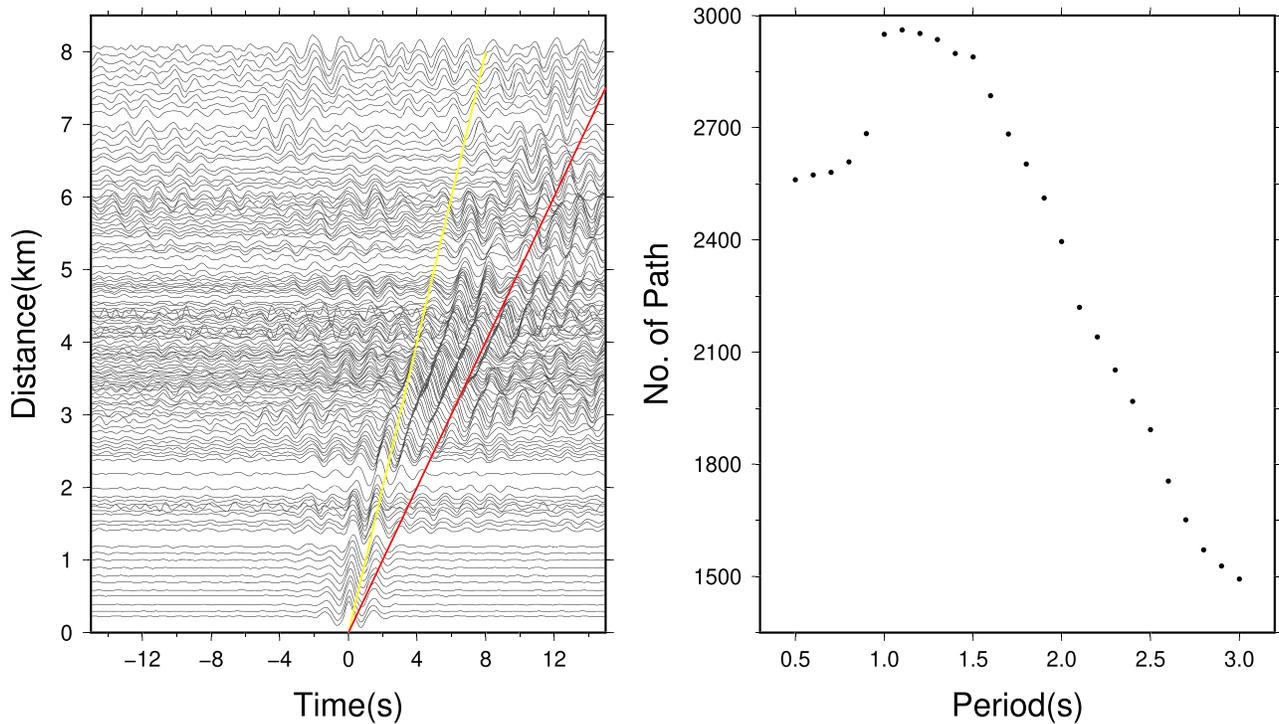
Figure 6. (left) Record section of ambient noise cross correlations between the northwestmost station with all other stations. Red and yellow lines indicate arrivals of wave velocities in 0.5 and 1.0 km/s, respectively. (right) Number of paths in different periods after quality control used for the ambient noise tomography.

and location as marked by *P* waves (Figure 5b). In addition, the amplitudes of *S* wave train inside the LVZ are much larger than those outside. Next we inspected and calculated the average travel time delays for *S* waves of the six teleseismic earthquakes with the reference station in the northwest end of the array. Error bars for *S* waves were larger than those of *P* waves, (Figure 5c). However, the distinct feature was the existence of a LVZ of ~3.4 km in width.

3.2. Ambient Noise Tomography

Next we quantified the FZ velocity structure by conducting ambient noise tomography to obtain the *S* wave velocity model. The data processing procedures were similar to the standard noise cross-correlation processing (Bensen et al., 2007; Shapiro et al., 2005; Yang et al., 2010; Yao et al., 2006). We first cut the data into half-hour segment, then decimated the sampling rate to 20 Hz. After detrending and removing the instrument response, we filtered the data in the period band from 0.5 to 5 s. In order to reduce the effect of earthquake signals and the peak in the frequency domain, temporal normalization and spectral whitening were adopted. Using the processed waveforms, we performed cross correlations for all station pairs and stacked the positive and negative lags to improve the SNR. Figure 6(left) showed an example of stacked cross correlagrams with respect to the reference station in the northwest end of the array. Clear signals were observed with move outs corresponding to wave velocities of 0.5–1 km/s (Figure 6, left).

Rayleigh wave group velocity dispersion curves were measured by frequency-time analysis (FTAN) from the cross correlagrams (Yao et al., 2006). Since the station spacings were small, we cannot distinguish the phase velocity dispersion curve. In order to obtain a reliable tomography result, the following data quality control criteria were applied to identify and reject bad measurements. First of all, we deleted the dispersion curves with interstation spacing less than 1.5 wavelengths at each period. The period-dependent SNR was regarded as the peak in a signal window divided by the root-mean-square of the trailing noise. We only kept the dispersion measurements whose SNRs were larger than 6. As such, we obtained ~1,500–3,000 dispersion measurements for periods ranging from 0.5 to 3.0 s (Figure 6, right). We then derived the subsurface structure using a direct 3-D surface-wave tomography method, which skipped intermediate steps of inversion for
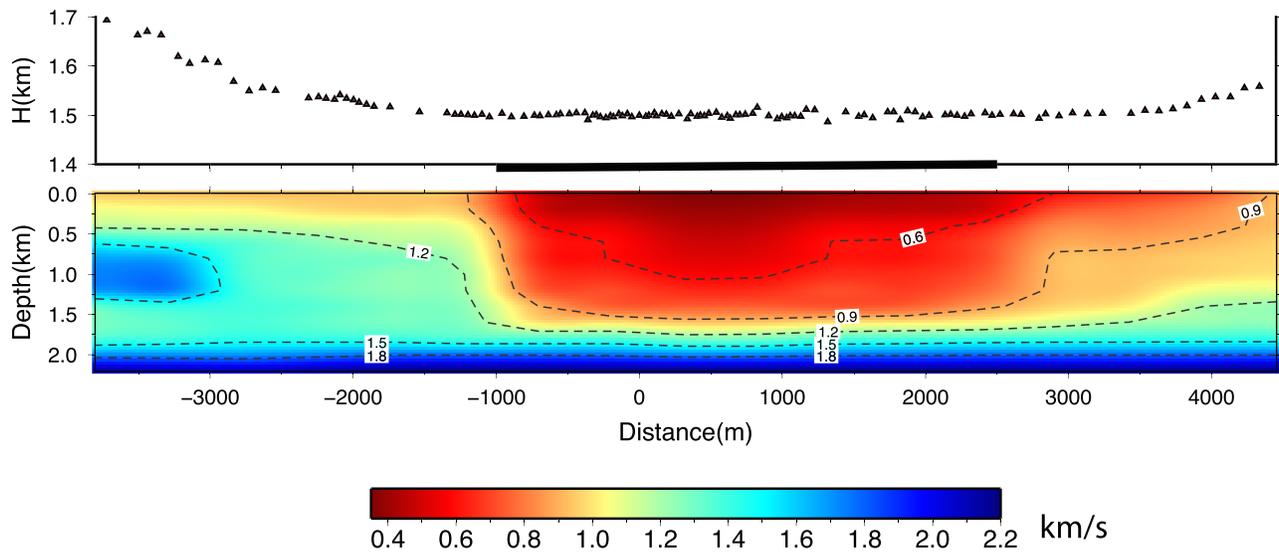
Figure 7. The top panel shows the station altitudes and locations from northwest to southeast. Black bar marks the low-velocity zone inferred from teleseismic *P* waves. The bottom panel shows shear wave velocity model beneath the array derived from ambient noise tomography.

phase- or group-velocity maps and considered ray bending effects on surface-wave tomography in a complex medium (Fang et al., 2015; Li et al., 2016).

In the final shear-wave velocity image (Figure 7b), we found a clear LVZ that was well captured by the dense array (Figure 7a), centering around the geologically inferred fault trace. The velocity was faster in the northwestern side of the LVZ than that in the southeast. Within the LVZ, V_s was ~600 m/s extending to 1 km, reduced by ~60% and ~40% compared with the host rock in the northwestern and southeastern side of the LVZ. If we tracked the velocity contour of 600 m/s, the LVZ width was ~3.7 km (Figure 7b), slightly larger than what was inferred from teleseismic *P* waves (3.4 km). The LVZ extended to ~1.5 km in depth, with the bottom V_s of 1.2 km/s. We also derived depth sensitivity kernels for Rayleigh wave group velocities at five periods 0.5, 1.0, 1.7, 2.3, and 3.0 s (Figure 8), using the 1-D average velocity model across the entire array (Figure 8a). Apparently, longer period Rayleigh waves were sensitive to structure at greater depth. Short-period data of 0.5 s were most sensitive to subsurface ~100 m in depth. At ~3.0 s, our dispersion data showed good sensitivity to structures ~2.0 km in depth (Figure 8c). In comparison, the kernels showed that within the LVZ the sensitivity was only good to depths no more than 1 km (Figure 8d).

3.3. Comparison With Travel Times of Teleseismic *S* Waves

Although our depth sensitivity kernels confirmed that we can resolve the subsurface structure down to 2 km, we cannot rule out that the LVZ might extend to greater depth, beyond what we can resolve. To verify, we compared theoretical travel times of teleseismic *S* waves by incorporating the 2-D model on top of the IASP91 model. Here we focused on the differential times of direct *S* arrivals across the array so we derived a 1-D V_s model beneath each station at the top 2 km and then calculated the travel times. After obtaining the theoretical travel times of *S* waves, we corrected their array geometry effects and topography effects following the same process that was applied on the data. Eventually, we obtained the across-array differential times using the reference station in the northwest end of the array.

The across-array differential times of *S* waves after incorporating the 2-D model showed nearly constant in the northwest (Figures 5a and 5b), abruptly delayed starting from the profile at −1 km, and bounced back at the profile of 2.5 km. Such delay time patterns of *S* waves coincided with the boundaries that were indicated from *P* wave travel times (Figure 3). We then compared the average across-array differential times of *S* waves for the six teleseismic events with observations (Figure 5c). In both sides of the array outside the LVZ, the theoretical differential times matched well with observations. However, the theoretical differential times within the LVZ overpredicted the across-fault delay.
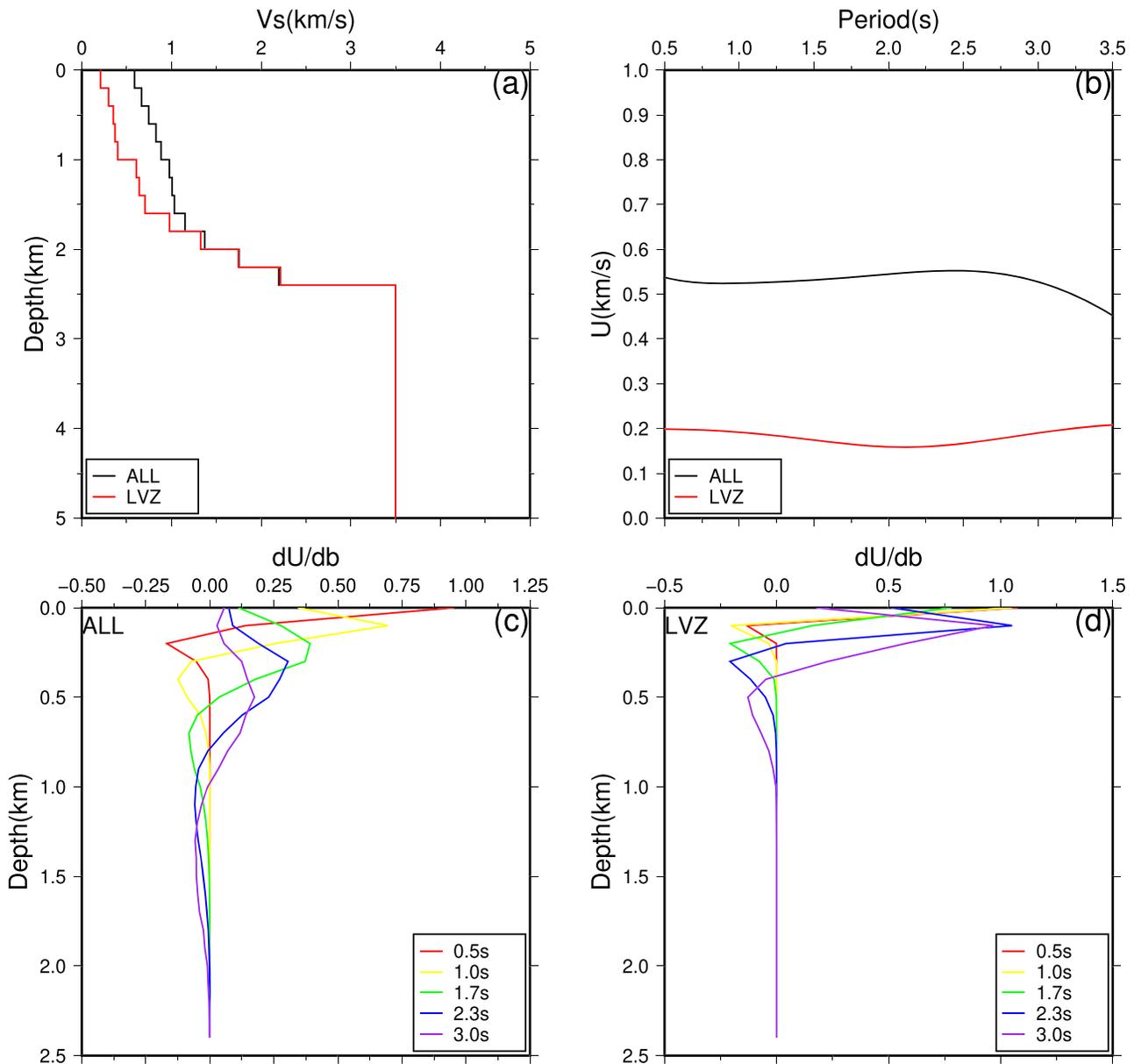
Figure 8. (a) Average shear wave velocity model within the low-velocity zone (red) and across the entire array (black) on top of the PREM model. (b) Group velocities from 0.5 to 3.5 s for the two averaged velocity models in panel (a). Depth sensitivity kernels for group velocities at five periods: 0.5 s (red line), 1.0 s (yellow line), 1.7 s (green line), 2.3 s (blue line), and 3.0 s (purple line) for the average shear wave model beneath the entire array (c) and within the low velocity zone (d).

Such overprediction may stem from a few factors. First, the teleseismic *S* waves were pretty noisy compared with *P* waves. Although the amplitudes of the *S* wave train were larger within the LVZ than those on stations outside, hand-picked direct *S* wave arrivals may contain considerable uncertainties that were reflected by the error bars (Figure 5c). Second, our LVZ model was derived from ambient noise tomography, a surface wave method, which might lead to differences in body wave predictions although the first-order feature kept the same. On the other hand, the overpredicted delay times of *S* waves provided independent and robust constraints on the LVZ depth, which should be no more than 2 km beneath the CHF. Otherwise, the travel times of teleseismic *S* waves should be further delayed. Such overprediction of S arrivals may also be caused by the fact that the LVZ structure at depth was affected by the smearing effects, as implied by the sensitivity kernels within the LVZ (Figure 8d). As such, the LVZ might be even shallower than 1.5 km.

4. Discussion

4.1. Width of the LVZ

Using travel times of teleseismic earthquakes and ambient noise tomography based on the dense array data, we found a ~3.4-km-wide LVZ associated with the Chenghai fault. To our best knowledge, such width of the LVZ was the largest among FZs that had been investigated by dense arrays. Usually fault damage zones were on the order of 100 m (e.g., Yang, 2015), especially those associated with recent ruptures. For instance, the LVZ on the ruptured fault of the 1992 M_w7.3 Landers earthquake was ~300 m in width (Li et al., 1994, 2007; Peng et al., 2003). The M_w7.1 Hector Mine earthquake produced a damage zone of 75–100 m in width along the Lavic Lake fault (Li et al., 2002). Such 100-m scale damage zones were also found by drilling projects on the San Andreas Fault near Parkfield (Li & Malin, 2008) and the Longmenshan Fault after the 2008 Wenchuan earthquake (Li et al., 2013). A LVZ wider than 1 km was rare, except the one along the Calico fault in the Eastern California Shear Zone, in between the 1992 Landers and 1999 Hector earthquake ruptured zones (Cochran et al., 2009; Yang et al., 2011). Since the Calico fault had not experienced large earthquakes in the past thousands of years, it had been interpreted as long-lived fault damages (Cochran et al., 2009).

However, seismic methods cannot distinguish fault damage zones or shallow sedimentary material, or other factors leading to a reduction in wave velocities near fault. Indeed, the CHF in the region was the controlling factor of Binchuan basin, which was formed during Quaternary. Beneath the array were mostly sediments from Quaternary alluvial fan deposits with mixture of sandstone (Huang et al., 2018). The CHF had an oblique motion with normal faulting and left-lateral strike-slip components, with estimated long-term slip rate of <1 mm/a. Despite the rather small slip rate, there had been a number of earthquakes with moderate to large magnitudes along the CHF. The largest earthquake was the 1515 $M7^3/_4$ earthquake in the northern portion of the CHF. In 1992, there were two earthquakes with magnitude of 5.1 and 5.4, respectively, in the nearby region. In the south, the largest one was the 1803 $M6^1/_4$ earthquake near the southern edge of the Binchuan basin. However, there were no evidences of historical earthquakes in the portion of the CHF where our dense array was deployed, so as to leave a seismic gap in the region (Huang et al., 2018). Therefore, we interpreted that the LVZ was the sediment controlled by the CHF, instead of fault damage zones.

Indeed, the entire Binchuan basin was mostly composing of lake source and river source deposits (Luo et al., 2015). Although our array was deployed primarily within the basin, sitting on the sediments, our tomographic images clearly showed lateral variation in the extent of subsurface sediment. Furthermore, there were along-strike variation in the LVZ structure within the basin, as revealed by teleseismic travel time anomalies that were sampled by a larger aperture 2-D array with average station spacing of ~2 km (Yang & Duan, 2019). To the north of our array, the LVZ signature was not that prominent (Yang & Duan, 2019). Such heterogeneous distribution of LVZ was probably attributed to the fluid dynamics, sediment source, and fault motion at different geological times. Regardless of the mechanism of its formation, such a ~3.4-km-wide LVZ would be significant for ground shaking during future earthquakes, considering the population in the Binchuan county (>340,000).

4.2. Constraining Depth Extent of the LVZ

It had long been in debate whether the fault damage zone extended to the base of the seismogenic zone (Li et al., 1997; Li & Vernon, 2001; Wu et al., 2010) or was limited to shallow depths, for example, a few kms below the surface (Allam et al., 2014; Lewis et al., 2005; Yang et al., 2011; Yang & Zhu, 2010; Zigone et al., 2014). Across-fault arrays in the early stage were mostly deployed in a small aperture, for example, less than 1–2 km in length, limiting techniques that were used to derive the subsurface structure. The most common one was the FZ trapped waves (Ben-Zion & Sammis, 2003; Li et al., 1990, 1994), which however led to controversial conclusions in depth extents of fault damage zones (Lewis et al., 2005; Li & Vernon, 2001; Wu et al., 2010). As more dense across-fault arrays became available in larger aperture and a large number of sensors, such as the Long Beach array (e.g., Lin et al., 2013; Schmandt & Clayton, 2013) and the 2-D San Jacinto Fault array (Ben-Zion et al., 2015), detailed FZ images had been obtained in high resolution, which mostly resolved LVZs extending to shallow depths only (e.g., Share et al., 2019).

Benefiting from our large aperture (>8 km) of the linear array across the CHF, we here constrained the LVZ depth from both ambient noise tomography and teleseismic travel times. Similar approach was conducted to derive internal structure of the San Jacinto fault zone at Blackburn Saddle, where a 2-km-long dense array was deployed (Share et al., 2019). Based on our S wave model derived from noise, there was a slight difference in V_s between the northwestern and southeastern sides of the CHF at the top 2 km. If such velocity difference continued to seismogenic depths, the bimaterial contrast might be important for future rupture propagation (Ampuero & Ben-Zion, 2008). Although our constrained LVZ was shallow, it would be able to modulate rupture propagation of future earthquakes (Weng et al., 2016), as did by other heterogeneities on faults, for example, seismogenic width (Chen & Yang, 2020; Weng & Yang, 2017), fault geometry (Yang et al., 2013; Yu et al., 2018), and heterogeneous stress distribution (Weng et al., 2015; Yang et al., 2012; Yang, Yao, He, & Newman, 2019; Yang, Yao, He, Newman, & Weng, 2019).

Besides constraining the shallow subsurface structure, coherent waveforms of teleseismic earthquakes also indicated a rather homogeneous crustal structure beneath our array at greater depths. Although our array was primarily targeting at imaging FZ structure, the data can be used to derive crustal structure. For instance, Moho interface can be delineated by autocorrelation and cross correlation of ambient noise across the array (She et al., 2019). Given the rapid growth of large N array, detailed crustal structure including FZs with well-resolved depth extents can be derived from such dense array data.

5. Conclusions

Using the waveform data recorded by a dense array we deployed across the southern portion of the Chenghai Fault in Yunnan, China, we derived high-resolution subsurface structure beneath the array. Our ambient noise tomographic results showed a distinct LVZ with a width of 3.4 km across the CHF. The LVZ extended to 1.5 km in depth and likely represents nonuniform distribution of sediments during the formation and evolution of Binchuan basin, to which the CHF was one of the controlling factors. Considering the large population in the Binchuan basin, the newly discovered wide LVZ associated with the CHF could be an important factor for seismic hazard assessment, as it may amplify ground motion in future earthquakes.

Data Availability Statement

Waveform data used in this study are available from Data Management Centre of China Seismic Experimental Site (http://www.cses.ac.cn).

References

Allam, A. A., Ben-Zion, Y., Kurzon, I., & Vernon, F. (2014). Seismic velocity structure in the Hot Springs and trifurcation areas of the San Jacinto Fault zone, California, from double-difference tomography. *Geophysical Journal International*, *198*(2), 978–999. https://doi.org/10.1093/gji/ggu176

Allen, C. R., Gillespie, A. R., Han, Y., Sieh, K. E., Zhang, B., & Zhu, C. (1984). Red River and associated faults, Yunnan Province, China: Quaternary geology, slip rates, and seismic hazard. *Geological Society of America Bulletin*, *95*(6), 686–700. https://doi.org/10.1130/0016-7606(1984)95%3C686:RRAAFY%3E2.0.CO;2

Ampuero, J.-P., & Ben-Zion, Y. (2008). Cracks, pulses and macroscopic asymmetry of dynamic rupture on a bimaterial interface with velocity-weakening friction. *Geophysical Journal International*, *173*(2), 674–692. https://doi.org/10.1111/j.1365-246X.2008.03736.x

Ampuero, J. P., Vilotte, J. P., & Sanchez-Sesma, F. (2002). Nucleation of rupture under slip dependent friction law: Simple models of fault zone. *Journal of Geophysical Research*, *107*(B12), 2324. https://doi.org/10.1029/2001JB000452

Bensen, G., Ritzwoller, M., Barmin, M., Levshin, A., Lin, F., Moschetti, M., et al. (2007). Processing seismic ambient noise data to obtain reliable broad-band surface wave dispersion measurements. *Geophysical Journal International*, *169*(3), 1239–1260. https://doi.org/10.1111/j.1365-246X.2007.03374.x

Ben-Zion, Y., & Sammis, C. G. (2003). Characterization of fault zones. *Pure and Applied Geophysics*, *160*(3), 677–715. https://doi.org/10.1007/PL00012554

Ben-Zion, Y., Vernon, F. L., Ozakin, Y., Zigone, D., Ross, Z. E., Meng, H., et al. (2015). Basic data features and results from a spatially dense seismic array on the San Jacinto fault zone. *Geophysical Journal International*, *202*(1), 370–380. https://doi.org/10.1093/gji/ggv142

Caine, J. S., Evans, J. P., & Forster, C. B. (1996). Fault zone architecture and permeability structure. *Geology*, *24*(11), 1025–1028. https://doi.org/10.1130/0091-7613(1996)024%3C1025:FZAAPS%3E2.3.CO;2

Chen, S., Wang, B., Tian, X., Wang, F., Liu, B., & Li, L. (2016). Wide angle reflection and refraction results in Yunxian-Ninglang, northwestern Yunnan, *Seismology and Geology*, *38*. https://doi.org/10.3969/j.issn.0253-4967.2016.01.00

Chen, X., & Yang, H. (2020). Effects of seismogenic width and low-velocity zones on estimating slip-weakening distance from near-fault ground deformation, *Earth and Space Science Open Archive*. https://doi.org/10.1002/essoar.10503380.1

Chen, Y., Wang, B., & Yao, H. (2017). Seismic airgun exploration of continental crust structures. *Science China Earth Sciences*, *60*(10), 1739–1751. https://doi.org/10.1007/s11430-016-9096-6

Cochran, E. S., Li, Y., Shearer, P. M., Barbot, S., Fialko, Y., & Vidale, J. E. (2009). Seismic and geodetic evidence for extensive, long-lived fault damage zones. *Geology*, *37*(4), 315–318. https://doi.org/10.1130/G25306A.1

Deng, Q. (2004). *Maps of Active Faults in China*. Beijing: Science Press.

Eberhart-Phillips, D., Stanley, W. D., Rodriguez, B. D., & Lutter, W. J. (1995). Surface seismic and electrical methods to detect fluids related to faulting. *Journal of Geophysical Research*, *100*(B7), 12,919–12,936. https://doi.org/10.1029/94JB03256

Fang, H., Yao, H., Zhang, H., Huang, Y.-C., & van der Hilst, R. D. (2015). Direct inversion of surface wave dispersion for three-dimensional shallow crustal structure based on ray tracing: Methodology and application. *Geophysical Journal International*, *201*(3), 1251–1263. https://doi.org/10.1093/gji/ggv080

Faulkner, D. R., Jackson, C. A. L., Lunn, R. J., Schlische, R. W., Shipton, Z. K., Wibberley, C. A. J., & Withjack, M. O. (2010). A review of recent developments concerning the structure, mechanics and fluid flow properties of fault zones. *Journal of Structural Geology*, *32*(11), 1557–1575. https://doi.org/10.1016/j.jsg.2010.06.009

Fohrmann, M., Igel, H., Jahnke, G., & Ben-Zion, Y. (2004). Guided waves from sources outside faults: An indication for shallow fault zone structure? *Pure and Applied Geophysics*, *161*(11-12), 2125–2137. https://doi.org/10.1007/s00024-004-2553-y

Harris, R. A., & Day, S. M. (1997). Effects of a low-velocity zone on a dynamic rupture. *Bulletin of the Seismological Society of America*, *87*, 1267–1280.

Hillers, G., Campillo, M., Ben-Zion, Y., & Roux, P. (2014). Seismic fault zone trapped noise. *Journal of Geophysical Research: Solid Earth*, *119*, 5786–5799. https://doi.org/10.1002/2014JB011217

Huang, X., Wu, Z., Huang, X., & Luo, R. (2018). Tectonic geomorphology constrains on the quaternary activity and segmentation along Chenghai-Binchuan fault zone in Northwest Yunnan, China. *Earth Science*, *43*(12), 4651. https://doi.org/10.3799/dqkx.2017.548

Huang, Y., & Ampuero, J. P. (2011). Pulse-like ruptures induced by low-velocity fault zones. *Journal of Geophysical Research*, *116*, B12307. https://doi.org/10.1029/2011JB008684

Huang, Y., Ampuero, J. P., & Helmberger, D. V. (2014). Earthquake ruptures modulated by waves in damaged fault zones. *Journal of Geophysical Research: Solid Earth*, *119*, 3133–3154. https://doi.org/10.1002/2013JB010724

Kennett, B. L. N., & Engdahl, E. R. (1991). Traveltimes for global earthquake location and phase identification. *Geophysical Journal International*, *105*(2), 429–465. https://doi.org/10.1111/j.1365-246x.1991.tb06724.x

Lewis, M. A., Peng, Z. G., Ben-Zion, Y., & Vernon, F. L. (2005). Shallow seismic trapping structure in the San Jacinto fault zone near Anza, California. *Geophysical Journal International*, *162*(3), 867–881. https://doi.org/10.1111/j.1365-246X.2005.02684.x

Li, C., Yao, H., Fang, H., Huang, X., Wan, K., Zhang, H., & Wang, K. (2016). 3D near-surface shear-wave velocity structure from ambient-noise tomography and borehole data in the Hefei urban area, China. *Seismological Research Letters*, *87*(4), 882–892. https://doi.org/10.1785/0220150257

Li, H., Wang, H., Xu, Z., Si, J., Pei, J., Li, T., et al. (2013). Characteristics of the fault-related rocks, fault zones and the principal slip zone in the Wenchuan earthquake fault scientific drilling project Hole-1 (WFSD-1). *Tectonophysics*, *584*, 23–42. https://doi.org/10.1016/j.tecto.2012.08.021

Li, H., Zhu, L., & Yang, H. (2007). High-resolution structures of the landers fault zone inferred from aftershock waveform data. *Geophysical Journal International*, *171*(3), 1295–1307. https://doi.org/10.1111/j.1365-246X.2007.03608.x

Li, Y., Aki, K., Adams, D., Hasemi, A., & Lee, W. H. K. (1994). Seismic guided waves trapped in the fault zone of the Landers, California, earthquake of 1992. *Journal of Geophysical Research*, *99*(B6), 11,705–11,722. https://doi.org/10.1029/94JB00464

Li, Y., Leary, P., Aki, K., & Malin, P. (1990). Seismic trapped modes in the Oroville and San Andreas fault zones. *Science*, *249*(4970), 763–766. https://doi.org/10.1126/science.249.4970.763

Li, Y., & Malin, P. E. (2008). San Andreas Fault damage at SAFOD viewed with fault-guided waves. *Geophysical Research Letters*, *35*, L08304. https://doi.org/10.1029/2007GL032924

Li, Y., & Vernon, F. L. (2001). Characterization of the San Jacinto fault zone near Anza, California, by fault zone trapped waves. *Journal of Geophysical Research*, *106*(B12), 30,671–30,688. https://doi.org/10.1029/2000JB000107

Li, Y., Vidale, J., & Cochran, E. (2004). Low-velocity damaged structure of the San Andreas Fault at Parkfield from fault zone trapped waves. *Geophysical Research Letters*, *31*, L12S06. https://doi.org/10.1029/2003GL019044

Li, Y., Vidale, J. E., Aki, K., Xu, F., & Burdette, T. (1998). Evidence of shallow fault zone strengthening after the 1992 *M* 7.5 Landers, California, earthquake. *Science*, *279*(5348), 217–219. https://doi.org/10.1126/science.279.5348.217

Li, Y., Vidale, J. E., Day, S. M., Oglesby, D. D., & the SCEC Field Working Team (2002). Study of the 1999 *M* 7.1 Hector Mine, California, earthquake fault plane by trapped waves. *Bulletin of the Seismological Society of America*, *92*(4), 1318–1332. https://doi.org/10.1785/0120000909

Li, Y. G., Vernon, F. L., & Aki, K. (1997). San Jacinto fault-zone guided waves: A discrimination for recently active fault strands near Anza, California. *Journal of Geophysical Research*, *102*(B6), 11,689–11,701. https://doi.org/10.1029/97JB01050

Lin, F., Li, D., Clayton, R. W., & Hollis, D. (2013). High-resolution 3D shallow crustal structure in Long Beach, California: Application of ambient noise tomography on a dense seismic array. *Geophysics*, *78*(4), Q45–Q56. https://doi.org/10.1190/GEO2012-0453.1

Luan, Y., Yang, H., & Wang, B. (2016). Large volume air-gun waveform data processing (I): Binchuan, Yunnan. *Earthquake Research China*, *32*(2), 305–318.

Luo, R., Wu, Z., Huang, X., Huang, X., Zhou, C., & Tian, T. (2015). The main active faults and the active tectonic system of Binchuan area, northwestern Yunnan. *Geological Bulletin of China*, *34*(1), 155–170.

Pelties, C., Huang, Y., & Ampuero, J.-P. (2015). Pulse-like rupture induced by three-dimensional fault zone flower structures. *Pure and Applied Geophysics*, *172*(5), 1229–1241. https://doi.org/10.1007/s00024-014-0881-0

Peng, Z., Ben-Zion, Y., Michael, A. J., & Zhu, L. (2003). Quantitative analysis of seismic fault zone waves in the rupture zone of the landers, 1992, California earthquake: Evidence for a shallow trapping structure. *Geophysical Journal International*, *155*(3), 1021–1041. https://doi.org/10.1111/j.1365-246X.2003.02109.x

Qiu, H., Ben-Zion, Y., Ross, Z. E., Share, P.-E., & Vernon, F. L. (2017). Internal structure of the San Jacinto fault zone at Jackass Flat from data recorded by a dense linear array. *Geophysical Journal International*, *209*(3), 1369–1388. https://doi.org/10.1093/gji/ggx096

Schmandt, B., & Clayton, R. W. (2013). Analysis of teleseismic *P* waves with a 5200-station array in Long Beach, California: Evidence for an abrupt boundary to inner borderland rifting. *Journal of Geophysical Research: Solid Earth*, *118*, 5320–5338. https://doi.org/10.1002/jgrb.50370

Shapiro, N. M., Campillo, M., Stehly, L., & Ritzwoller, M. H. (2005). High-resolution surface-wave tomography from ambient seismic noise. *Science*, *307*(5715), 1615–1618. https://doi.org/10.1126/science.1108339

Share, P.-E., Allam, A. A., Ben-Zion, Y., Lin, F., & Vernon, F. L. (2019). Structural properties of the San Jancinto fault zone at Blackburn Saddle from seismic data of a dense linear array. *Pure and Applied Geophysics*, *176*(3), 1169–1191. https://doi.org/10.1007/s00024-018-1988-5

Share, P.-E., Ben-Zion, Y., Ross, Z. E., Qiu, H., & Vernon, F. (2017). Internal structure of the San Jacinto fault zone at Blackburn Saddle from seismic data of a linear array. *Geophysical Journal International*, *210*(2), 819–832. https://doi.org/10.1093/gji/ggx191

She, Y., H. Yao, H. Yang, and J. Feng (2019), Retrieval of the P wave reflections across the Chenghai fault zone from the autocorrelation and cross-correlation of ambient seismic noise, AGU Fall Meeting Abstract No.S23C-0643

Vidale, J. E., & Li, Y. (2003). Damage to the shallow landers fault from the nearby Hector Mine earthquake. *Nature*, *421*(6922), 524–526. https://doi.org/10.1038/nature01354

Wang, B., Wu, G., Su, Y., Wang, B., Ge, H., Jin, M., et al. (2015). Site construction of the Binchuan transmitting seismic stations and preliminary observational data. *Journal of Seismology Research*, *38*(1), 1–6.

Wang, B., Yang, W., Wang, W., Yang, J., Li, X., & Ye, B. (2020). Diurnal and semidiurnal P and S wave velocity changes measured using an airgun source. *Journal of Geophysical Research: Solid Earth*, *125*, e2019JB018218. https://doi.org/10.1029/2019JB018218

Wang, Y., Lin, F.-C., & Ward, K. M. (2019). Ambient noise tomography across the Cascadia subduction zone using dense linear seismic arrays and double beamforming. *Geophysical Journal International*, *217*(3), 1668–1680. https://doi.org/10.1093/gji/ggz109

Weng, H., Huang, J., & Yang, H. (2015). Barrier-induced supershear ruptures on a slip weakening fault. *Geophysical Research Letters*, *42*, 4824–4832. https://doi.org/10.1002/2015GL064281

Weng, H., & Yang, H. (2017). Seismogenic width controls aspect ratios of earthquake ruptures. *Geophysical Research Letters*, *44*, 2725–2732. https://doi.org/10.1002/2016GL072168

Weng, H., & Yang, H. (2018). Constraining frictional properties on fault by dynamic rupture simulations and near-field observations. *Journal of Geophysical Research: Solid Earth*, *123*, 6658–6670. https://doi.org/10.1029/2017JB015414

Weng, H., Yang, H., Zhang, Z., & Chen, X. (2016). Earthquake rupture extents and coseismic slips promoted by damaged fault zones. *Journal of Geophysical Research: Solid Earth*, *121*, 4446–4457. https://doi.org/10.1002/2015JB012713

Wu, J., Hole, J. A., & Snoke, J. A. (2010). Fault zone structure at depth from differential dispersion of seismic guided waves: Evidence for a deep waveguide on the San Andreas Fault. *Geophysical Journal International*, *182*, 343, no–354. https://doi.org/10.1111/j.1365-246X.2010.04612.x

Yang, H. (2015). Recent advances in imaging crustal fault zones: A review. *Earthquake Science*, *28*(2), 151–162. https://doi.org/10.1007/s11589-015-0114-3

Yang, H., & Duan, Y. (2019). High-resolution crustal structure illuminated by ultra-dense array recordings. *Acta Geologica Sinica*, *93*, 284. https://doi.org/10.1111/1755-6724.14094

Yang, H., Li, Z., Peng, Z., Ben-Zion, Y., & Vernon, F. (2014). Low velocity zones along the San Jacinto Fault, Southern California, from body waves recorded in dense linear arrays. *Journal of Geophysical Research: Solid Earth*, *119*, 8976–8990. https://doi.org/10.1002/2014JB011548

Yang, H., Liu, Y., & Lin, J. (2012). Effects of subducted seamounts on megathrust earthquake nucleation and rupture propagation. *Geophysical Research Letters*, *39*, L24302. https://doi.org/10.1029/2012GL053892

Yang, H., Liu, Y., & Lin, J. (2013). Geometrical effects of a subducted seamount on stopping megathrust ruptures. *Geophysical Research Letters*, *40*, 2011–2016. https://doi.org/10.1002/grl.50509

Yang, H., Yao, S., He, B., & Newman, A. (2019). Earthquake rupture dependence on hypocentral location along the Nicoya Peninsula subduction megathrust. *Earth and Planetary Science Letters*, *520*, 10–17. https://doi.org/10.1016/j.epsl.2019.05.030

Yang, H., Yao, S., He, B., Newman, A., & Weng, H. (2019). Deriving rupture scenarios from interseismic locking distributions along the subduction megathrust. *Journal of Geophysical Research: Solid Earth*, *124*, 10,376–10,392. https://doi.org/10.1029/2019JB017541

Yang, H., & Zhu, L. (2010). Shallow low-velocity zone of the San Jacinto fault from local earthquake waveform modeling. *Geophysical Journal International*, *183*(1), 421–432. https://doi.org/10.1111/j.1365-246X.2010.04744.x

Yang, H., Zhu, L., & Cochran, E. S. (2011). Seismic structures of the calico fault zone inferred from local earthquake travel time modelling. *Geophysical Journal International*, *186*(2), 760–770. https://doi.org/10.1111/j.1365-246X.2011.05055.x

Yang, Y., Zheng, Y., Chen, J., Zhou, S., Celyan, S., Sandvol, E., et al. (2010). Rayleigh wave phase velocity maps of Tibet and the surrounding regions from ambient seismic noise tomography. *Geochemistry, Geophysics, Geosystems*, *11*, Q08010. https://doi.org/10.1029/2010GC003119

Yao, H., van der Hilst, R. D., & de Hoop, M. V. (2006). Surface-wave array tomography in SE Tibet from ambient seismic noise and two-station analysis—I. Phase velocity maps. *Geophysical Journal International*, *166*(2), 732–744. https://doi.org/10.1111/j.1365-246X.2006.03028.x

Yao, S., & Yang, H. (2020). Rupture dynamics of the 2012 Nicoya M_w 7.6 earthquake: Evidence for low strength on the Megathrust. *Geophysical Research Letters*, *47*, e2020GL087508. https://doi.org/10.1029/2020GL087508

Yehya, A., Yang, Z., & Rice, J. R. (2018). Effect of fault architecture and permeability evolution on response to fluid injection. *Journal of Geophysical Research: Solid Earth*, *123*, 9982–9997. https://doi.org/10.1029/2018JB016550

Yu, H., Liu, Y., Yang, H., & Ning, J. (2018). Modeling earthquake sequences along the Manila subduction zone: Effects of three-dimensional fault geometry. *Tectonophysics*, *733*, 73–84. https://doi.org/10.1016/j.tecto.2018.01.025

Yu, W., Zhang, J., Zhou, G., Wang, J., & Zeng, X. (2005). Surface rupture of the 2001 Yongsheng *M*6 earthquake and Chenghai fault. *Journal of Seismology Research*, *28*(2), 125–128.

Zhang, Y., & Liu, J. (2016). Study on characteristics of fault activity and relation between fault activity and earthquakes in Yunnan region, *Journal of Geodesy and Geodynamics*, v. *36*(6), 485–489. https://doi.org/10.14075/j.jgg.2016.06.004

Zhou, Q., Guo, S., & Xiang, H. (2004). Principle and method of delineation of potential seismic sources in northeastern Yunnan province. *Seismology and Geology*, *26*(4), 761–771.

Zigone, D., Ben-Zion, Y., Campillo, M., & Roux, P. (2014). Seismic tomography of the Southern California plate boundary region from noise-based Rayleigh and love waves. *Pure and Applied Geophysics*, *172*(5), 1007–1032. https://doi.org/10.1007/s00024-014-0872-1

Zigone, D., Ben-Zion, Y., Lehujeur, M., Campillo, M., Hillers, G., & Vernon, F. L. (2019). Imaging subsurface structures in the San Jacinto fault zone with high-frequency noise recorded by dense linear arrays. *Geophysical Journal International*, *217*(2), 879–893. https://doi.org/10.1093/gji/ggz069